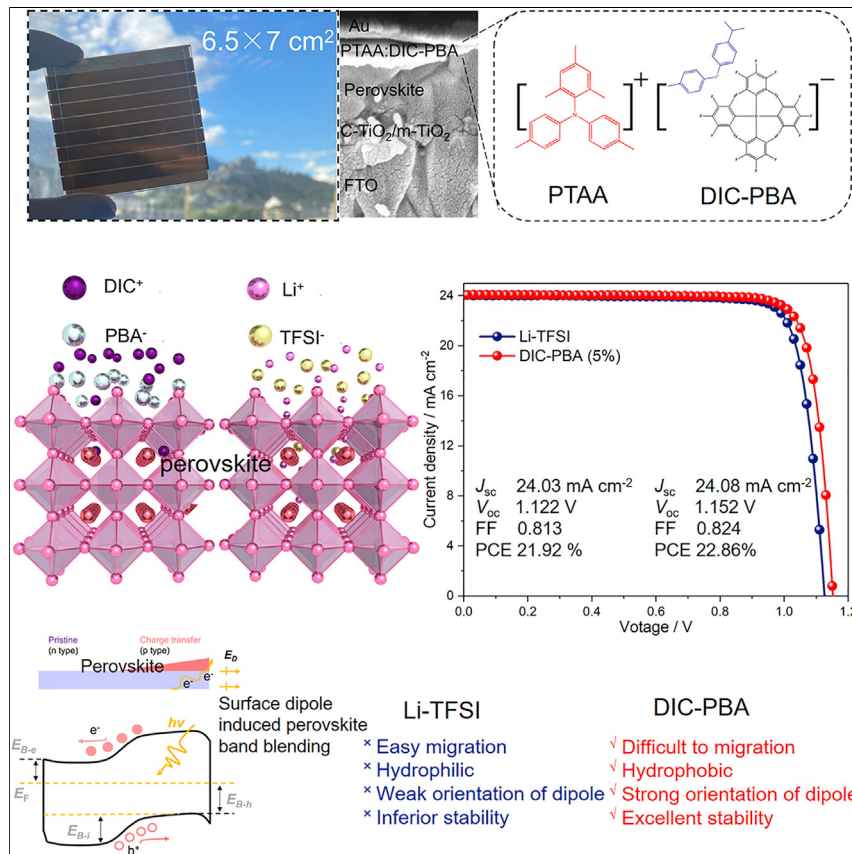


Article

Tailoring electric dipole of hole-transporting material p-dopants for perovskite solar cells



An interfacial dipole-oriented organic salt dopant was demonstrated as an alternative to the Li-TFSI/t-BP and applied to the small devices and large-area module (6.5 × 7 cm²; aperture area is 33.2 cm²), achieving high power conversion efficiency (PCE) of 22.86% and 19.13%, respectively. Additionally, it performed with significantly improved long-term stability up to 1,200 h.

Jianxing Xia, Yi Zhang,
Chuanxiao Xiao, ..., Abdullah M.
Asiri, Chunyang Jia, Mohammad
Khaja Nazeeruddin

cyjia@uestc.edu.cn (C.J.)
mdkhaja.nazeeruddin@epfl.ch (M.K.N.)

Highlights

Efficient doping of PTAA via regulatory molecular dipole

Surface doping of perovskite via oriented dipole

Trap states restrain via the oriented dipole

High efficiency of modules based on PTAA

Article

Tailoring electric dipole of hole-transporting material p-dopants for perovskite solar cells

Jianxing Xia,^{1,2,11} Yi Zhang,^{2,11} Chuanxiao Xiao,⁷ Keith Gregory Brooks,² Min Chen,⁷ Junsheng Luo,¹ Hua Yang,³ Nadja Isabelle Desiree Klipfel,² Jihua Zou,⁹ Yu Shi,¹ Xiaojun Yao,⁴ Jiangzhao Chen,⁵ Joseph M. Luther,⁷ Hongzhen Lin,⁸ Abdullah M. Asiri,⁶ Chunyang Jia,^{1,*} and Mohammad Khaja Nazeeruddin^{2,10,12,*}

SUMMARY

Li-TFSI/t-BP are the most widely employed p-dopants for hole-transporting materials (HTMs) within the state-of-the-art perovskite solar cells (PSCs). The hygroscopicity and migration of these dopants, however, lead to devices with limited stability. To solve this problem, we report here on a diphenyl iodide cation and pentafluorophenyl boric acid anion-based dopant (DIC-PBA) with an oriented interfacial dipole moment as an alternative to Li-TFSI/t-BP. Theoretical and experimental data reveal that DIC-PBA exhibits deep doping of poly[bis(4-phenyl)(2,4,6-triMethylphenyl)aMine] (PTAA) and also creates p-doping of perovskite surface, which originates from ionic interactions-derived dipole arrangement that yields fast interfacial charge transport. The improved intrinsic stability of PSCs originates from the inhibition of dipole moment degeneration on the perovskite surface. Devices prepared with DIC-PBA yielded high efficiency of 22.86%, and the modules (aperture area: 33.2 cm²) efficiency reached 19.13%. Importantly, the storage stability also significantly improved exceeding to 90% after aging 1,200 h under air ambient.

INTRODUCTION

Organic-inorganic hybrid perovskite-based solar cells (PSCs) have drawn significant attention because of the rapid increase in power conversion efficiency (PCE) since 2009.^{1–14} In state-of-the-art n-i-p PSCs, the π -conjugated polymer poly[bis(4-phenyl)(2,4,6-triMethylphenyl)aMine] (PTAA) and a small molecule 2,2',7,7'-Tetraakis[N,N-di(4-methoxyphenyl)amino]-9,9'-spirobifluorene (Spiro-OMeTAD) are widely used as p-type organic semiconductors, which facilitate hole extraction from the perovskite absorber.^{15,16} Both of these hole-transporting materials (HTMs) are commonly doped with bis(trifluoromethane)sulfonamide lithium salt (Li-TFSI) and 4-tert-butylpyridine (t-BP) to improve their hole mobility and work function (W_F). Despite the significant improvement in PCE achieved with these dopants, some drawbacks exist that prejudice the long-term stability of PSCs. The stability of PSC is now the most challenging issue that limits their commercialization. The Li-TFSI is a hydrophilic ionic compound, which adsorbs water from ambient air, resulting in aggregation of the lithium salt and a concurrent rapid degradation of the hole transportation layer (HTL) and decomposition of the perovskite layer via molecular diffusion from the HTL.^{17,18} In addition, the interfacial t-BP will also cause chemical decomposition of the perovskite by forming a [PbI₂-t-BP] coordinated complex over time, which further diminishes the long-term stability of PSCs.^{19,20} Thus, several groups

Context & scale

The doping of organic HTMs is significant in a broad range of electronic applications, including photovoltaics, transistors, and organic light-emitting diodes, especially influencing the performance and stability of PSCs. Herein, a metal-free cation united with a fluorine-containing anion is developed as an efficient p-dopant for PTAA, which changed the molecule dipole moment and ionic orientation on perovskite surface compared with Li-TFSI via altered ionic radius and interaction difference of both anion and cation on the perovskite surface. As a result, the PSCs deliver high efficiency of 22.86% (small area) and 19.13% (module, aperture area: 33.2 cm²) with enhanced stability. These results inspire bright futures for efficient p-dopants design within HTMs and open new avenues to stable PSC fabrication.

have now reported on alternative p-dopants based on ionic liquids,^{17,21} acid and inorganic salts,^{22,23} fullerene derivatives,^{18,24} and metal-organic frameworks^{25,26} to improve the stability and PCE of PSCs. However, these reports focused primarily on improving the hydrophobicity of the p-dopants, which determined the external stability of devices. In contrast, the Li⁺ ion always migrates to different layers of PSCs due to low migration barriers through perovskite, causing random doping and alteration of the charge equilibrium in PSCs.^{23,27-29} As a consequence, the efficiency of PSCs decreases during long-term aging. To alleviate the Li⁺ migration problem, metal sulfides have been introduced into the HTL, thus inhibiting the Li⁺ ion motion via the strong interaction of the Li-S bond, thereby improving the stability of PSCs.²³ Despite this significant progress in HTL p-dopant and additive research, the relevant contact interface is rarely explored in p-dopant design. The interface is compromised by interfacial barriers and uncoordinated perovskite surface defects that result in interfacial charge accumulation and recombination, thereby severely diminishing the intrinsic stability and performance.³⁰⁻³³ Furthermore, these surface and interfacial problem will be more seriously within the upscaling module devices due to the amplification effect. Thus, the influences of p-dopant on the interfacial contact and uncoordinated perovskite surface defects should be explored and taken into consideration in the design of efficient and stable p-dopants.

Herein, a diphenyl iodide cation and pentafluorophenyl boric acid anion-based dopant (DIC-PBA) is developed as an efficient and stable p-dopant for PTAA. The dopant of DIC-PBA exhibits a tuned, molecular dipole moment and a preferential ionic orientation on the perovskite surface compared with Li-TFSI. This arises from an altered ionic radius and interaction difference of both anion and cation on the perovskite surface. Compared with Li-TFSI, the DIC-PBA exhibits excellent hydrophobicity and does not easily migrate, which diminishes the ingress of moisture and maintains the surface dipole stable during aging. Both n-i-p-type small area and series-interconnected modules (aperture area: 33.2 cm²) realized with DIC-PBA dopant achieved efficiencies of 22.86% and 19.13%, respectively. We believe that both module and small cell efficiency values are the one of the highest reported to date for n-i-p structured PSCs based on PTAA. The cells also display much higher long-term stability up to 1,200 h under ambient conditions without encapsulation (retain over 90%; however, the Li-TFSI based degenerated to 45% of initial efficiency). We believe that this work will provide new insights and indicate a new direction in the development of stable and efficient HTM dopant design for PSCs.

RESULTS AND DISCUSSION

As illustrated in Figure 1A, in addition to the notorious hydrophilicity of the Li-TFSI dopant, which always dominated the external stability of PSCs, the small radius of Li⁺ (0.7 Å) can easily migrate to other functional layers and damage the intrinsic stability of devices due to the resulting random doping (Figure 1Aii). Conversely, if a Li-free large radius ionic dopant is developed for PSCs, it may significantly improve the PSC's intrinsic and external stability (Figure 1Ai). The large van der Waals radius of methyl diphenyl iodide cation (16.4 Å) not only exhibits the advantages of hydrophobicity and possible higher ion migration barrier (Figure S1) but also will increase the molecular dipole moment due to the larger distance between the ionic charge centers, which may result in strong electron acceptance and p-doping when in contact with PTAA. To enhance the dopant dipole moment and coulombically compensate for PTAA radicals after doping, the large van der Waals radius of the highly electro-negative fluorine-containing anion (pentafluorophenyl boric acid anion; 13.75 Å) was selected and combined with DIC-PBA in this work (Figure 1B).

¹State Key Laboratory of Electronic Thin Films and Integrated Devices, School of Electronic Science and Engineering, University of Electronic Science and Technology of China, Chengdu 610054, China

²Institute of Chemical Sciences and Engineering, École Polytechnique Fédérale de Lausanne (EPFL), Sion 1951, Switzerland

³Institute of High Energy Physics, Chinese Academy of Sciences (CAS), Beijing 100049, China

⁴State Key Laboratory of Applied Organic Chemistry, Lanzhou University, Lanzhou 730000, China

⁵Key Laboratory of Optoelectronic Technology and Systems, College of Optoelectronic Engineering, Chongqing University, Chongqing 400044, China

⁶Center of Excellence for Advanced Materials Research (CEAMR), King Abdulaziz University, P.O. Box 80203, 21589 Jeddah, Saudi Arabia

⁷National Renewable Energy Laboratory, Golden, CO 80401, USA

⁸i-Lab, Suzhou Institute of Nano-Tech and Nano-Bionics, Chinese Academy of Sciences, Suzhou 215123, China

⁹Institute of Fundamental and Frontier Sciences, University of Electronic Science and Technology of China, Chengdu 610054, China

¹⁰Department of Materials Science and Engineering, City University of Hong Kong, Kowloon, Hong Kong

¹¹These authors contributed equally

¹²Lead contact

*Correspondence: cyyia@uestc.edu.cn (C.J.), mdkhaja.nazeeruddin@epfl.ch (M.K.N.)

<https://doi.org/10.1016/j.joule.2022.05.012>

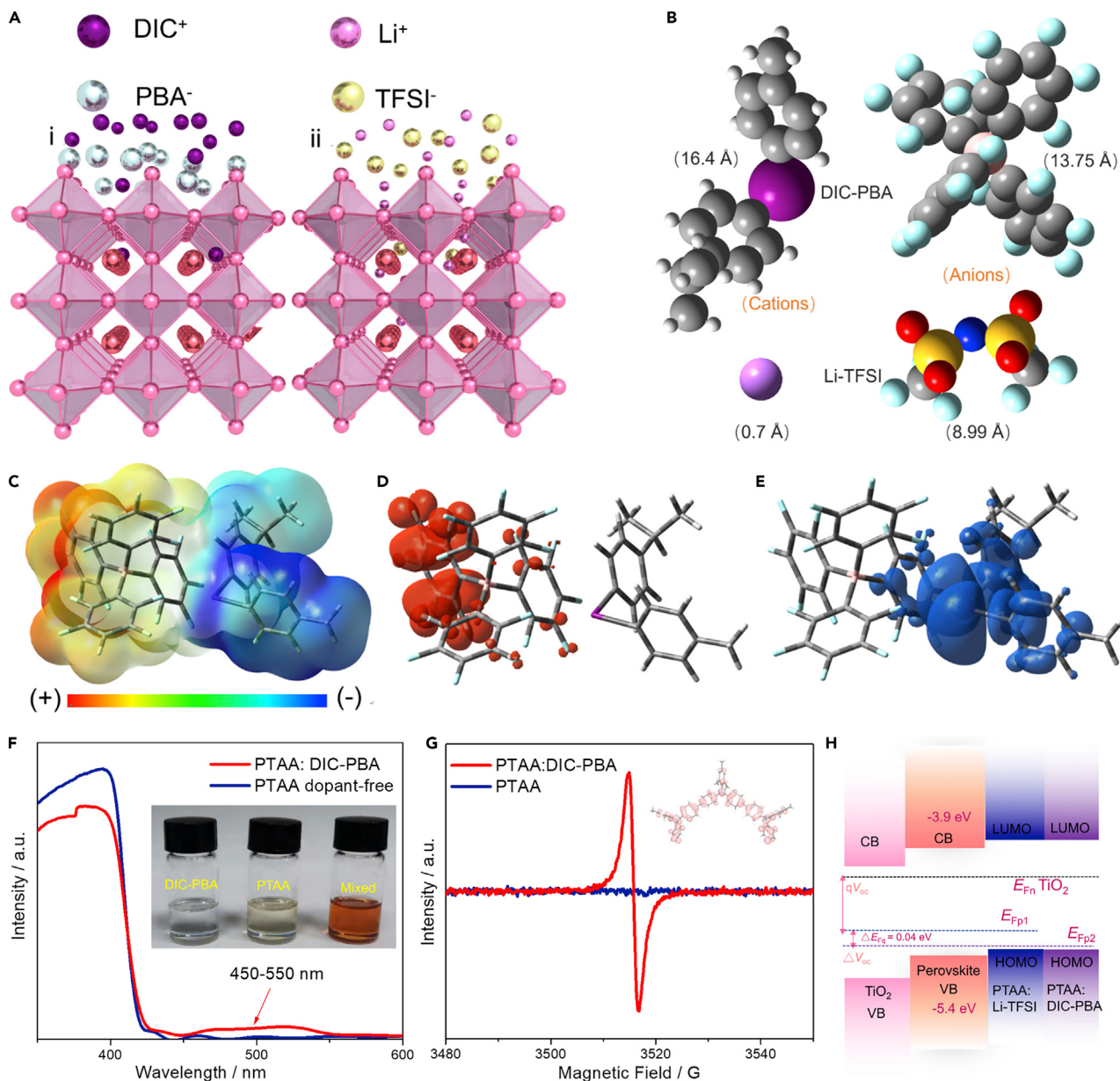


Figure 1. The efficient p-doping of PTAA

- (A) Illustration of Li-TFSI and DIC-PBA interactions with the perovskite surface.
- (B) The van der Waals surface of the Li⁺, DIC⁺, TFSI⁻, and PBA⁻ ions within both dopants.
- (C–E) (C–E), respectively, represent the electrostatic potential (ESP) of DIC-PBA dopant (the scale bars of ESP are –0.05–0.05), the localized hole (in red) and electron (in blue) under the highest occupied molecular orbital (HOMO), and the lowest unoccupied molecular orbital (LUMO) states. The pink, dark purple, gray, white, and cyan colors, respectively, represent the B, I, H, C, and F atoms.
- (F) The UV-vis absorption spectra of dopant-free and DIC-PBA-doped PTAA.
- (G) The ESR spectra of dopant-free PTAA and DIC-PBA (5%)-doped PTAA and the electron spin density of PTAA.
- (H) The illustration of energy shift of PTAA when doped with Li-TFSI or DIC-PBA after contact within devices.

To thoroughly analyze the hypothesis, the PTAA was first blended with DIC-PBA in toluene (TL) solvent, which may further improve the stability due to the absence of t-BP and acetonitrile. When the DIC-PBA was added into the PTAA solution (Figure 1F), the solution immediately turned reddish-brown, and an additional absorption peak in the range of 450–550 nm was observed. This peak is characteristic of

the $[PTAA]^{+}$ radical via the charge transfer between polymer and dopant.²⁰ To further confirm the possible electron transfer effect and the formation of this radical, the electron spin resonance (ESR) spectra were measured for DIC-PBA-doped PTAA and dopant-free PTAA solutions (Figure 1G). It was evident that the doped solution exhibited intense paramagnetic peaks at 3,510–3,520 G, which were absent for the un-doped material. These paramagnetic peaks verify the presence of the $[PTAA]^{+}$ radical. Furthermore, the calculation of electron spin density indicated widespread unpaired electrons over the entire $[PTAA]^{+}$ radical, which means the electrical conductivity will be improved in the presence of the radical.¹⁸ Thus, the electrical conductivity was probed by conductive atomic force microscopy (c-AFM), and the result showed that the sample doped with DIC-PBA displays strong current fluctuations compared with the Li-TFSI based film (Figure S2), which further shows the efficient doping by DIC-PBA.

A discussion of the mechanism of radical generation by doping follows. First, the electronic properties of DIC-PBA and PTAA (simplified to two monomer units) were studied by density functional theory (DFT) and the calculations and shown in Figures 1C–1E and S3. It is evident from the ground-state orbitals that there is a separated electron-hole pair over the entire DIC-PBA molecule and that the hole (red) is dominantly localized at the pentafluorophenyl boric acid anion components; nevertheless, the electron (blue) is localized on the methyl diphenyl iodide cation, which may derive from the strong molecular dipole moment (23.26 Debye; Figure 1C) due to the non-overlapping B^- and I^+ charge sites. The PTAA molecule displays an inconspicuous separation of charge, which may originate from the weak dipole (1.74 Debye) around the entire molecule (Figure S3). However, the charge distribution of ground-state orbitals within PTAA become separated when contact is made with the DIC-PBA dopant, and the electron (blue) localized at the methyl diphenyl iodide cation inverse to the hole (red), which accumulates over the entire PTAA molecule. This is attributed to the extra electric field arising from the intermolecular dipole moment (21.34 Debye; Figure S3) between the PTAA core and dopant. It is analogous to the intramolecular charge transfer behavior of DIC-PBA and further validates that the dipole moment is important for the charge transfer process. As shown in Figure S4, the charge density difference ($\Delta\rho$) is further calculated to directly observe the charge transfer process. The blue and yellow, respectively, are the electron depletion and accumulation. The electron dominantly accumulates at the contact interface and primarily concentrates on the side of the methyl diphenyl iodide cation, in agreement with the preceding analysis. Therefore, the doping is probability derived from the intermolecular dipole between the PTAA core and the methyl diphenyl iodide cation. However, the pentafluorophenyl boric acid anion components interact with the $[PTAA]^{+}$ radical to maintain the charge compensation (Figure S4).

In ionic doping systems, the W_F of an organic semiconductor is calculated from the sum of μ and χ ($\Delta\varphi = \mu + \chi$). Here, the μ indicates the electrochemical potential of carriers at the Fermi level and is always governed by the electronic structure of the organic semiconductor core. The χ is the surface dipole potential supplied by surface ionic layering and dipole effects.^{34,35} The large dipole moment of DIC-PBA dopant may create deep doping and a shift of the W_F . Ultraviolet photoelectron spectroscopy (UPS) is used to explore the dopant influence on the energy level of PTAA. The onsets (E_{onset}) and W_F regions of UPS based on Li-TFSI and DIC-PBA are compared in Figure S5. The $\Delta\varphi$ of PTAA doped with DIC-PBA (4.69 eV) is higher than that of Li-TFSI (4.65 eV) in accordance with the narrower energetic gap between the highest occupied molecular orbital (HOMO) and Fermi levels (E_F) as observed

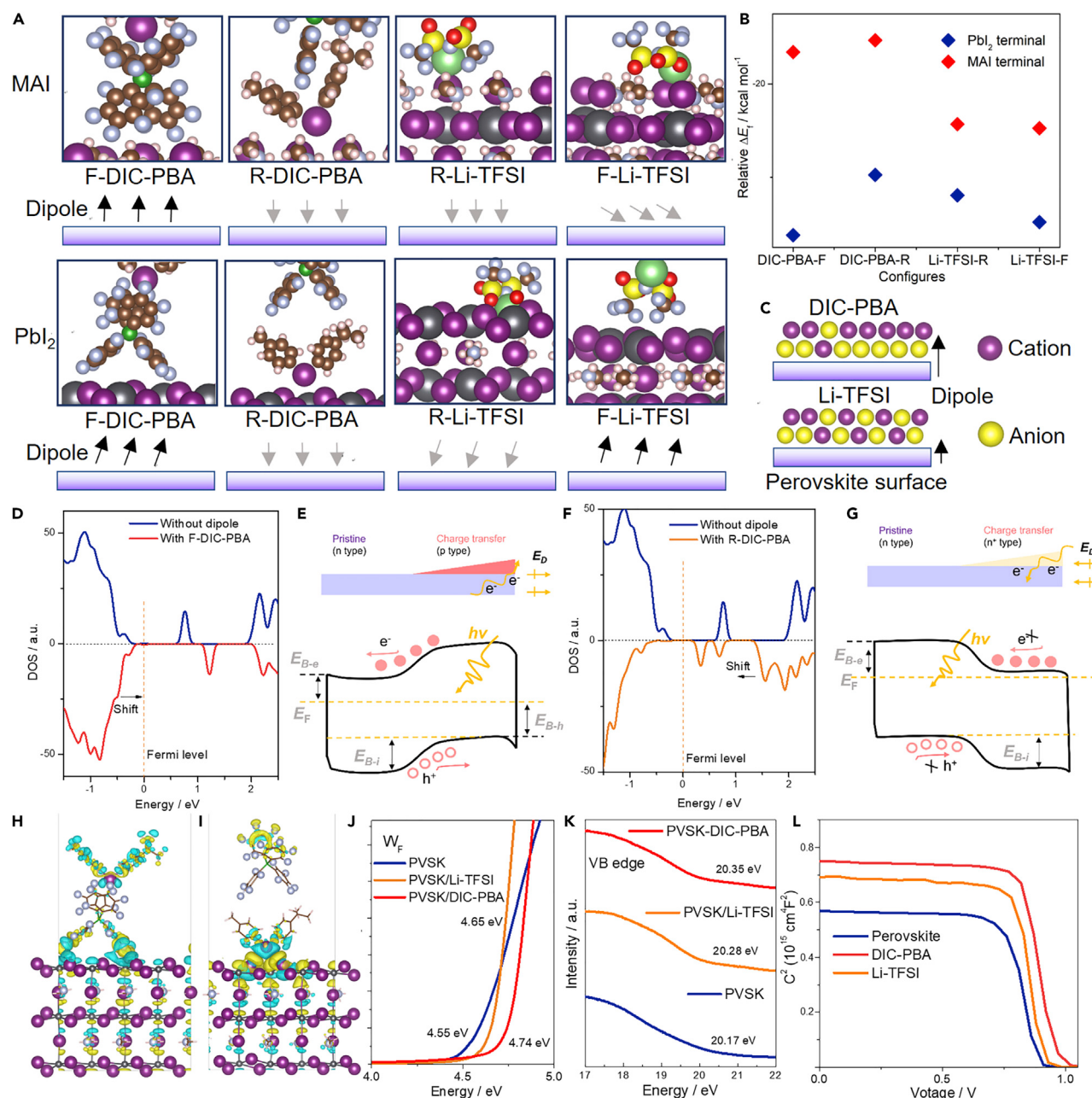


Figure 2. Surface doping via oriented dipole

(A) The optimized geometries of Li-TFSI and DIC-PBA adsorbed on perovskite surface (MAI and PbI₂ terminated) at forward (F) and reverse (R) orientation, as well as the corresponding illustration of the surface dipole orientation. The red, yellow, light pink, gray (molecule), black, dark green, light green, purple, and brown colors, respectively, represent the O, S, H, F, Pb, B, Li, I, and C atoms.

(B) The binding energy of the differently oriented Li-TFSI and DIC-PBA adsorbed on the perovskite surface.

(C) The illustration of dipole orientation of both Li-TFSI and DIC-PBA on perovskite surface.

(D) and (F) (D) and (F) represent, respectively, the density of states (DOS) of perovskite after interaction with the F and R-oriented DIC-PBA.

(E) and (G) (E) and (F) illustrate the corresponding energy level changes based on these differently oriented surface dipoles; the Fermi level was set as zero.

(H) The charge density difference of F-oriented DIC-PBA adsorbed on PbI₂ termination of perovskite (001) surface.

Figure 2. Continued

- (I) The charge density difference of R-oriented DIC-PBA adsorbed on PbI_2 termination of perovskite (001) surface, and the yellow and blue colors represent the charge accumulation ($\Delta\rho > 0$, positive) and depletion ($\Delta\rho < 0$, negative).
- (J and K) (J) and (K) are, respectively, the W_F and onset energy (E_{onset}) regions of UPS with or without the modified by Li-TFSI and DIC-PBA.
- (L) The Mott-Schottky plots as a function of applied bias at 10 kHz for the devices with Li-TFSI and DIC-PBA dopant modified perovskites under dark conditions.

from the E_{onset} region. These experimental and theoretical results confirm the efficient p-doping by the organic DIC-PBA provided by intermolecular electron transfer. The energetic alignment after the DIC-PBA and Li-TFSI doping, which balances E_F , is compared in Figure 1H. Similar energy levels are observed for both Li-TFSI doped PTAA. In addition, the devices show a larger split of quasi-Fermi level ($\Delta E_{Fq} \approx 0.04$ eV) between the TiO_2 film and PTAA when the DIC-PBA is employed as the dopant. The higher split of the quasi-Fermi level may be beneficial to the open-circuit voltage (V_{oc}) of devices.^{36,37}

The surface electronic properties of the perovskite/HTM heterojunction interface are vital for carrier transport. However, the semiconductor surface contact is usually tuned by the adsorbed organic molecule and ionic charge layers via surface or molecular electron transfer, facilitating or suppressing the interfacial free-charge transport.^{30,31,38} To investigate the influence of the dopant on the perovskite surface, first, the behavior of both DIC-PBA and Li-TFSI adsorption on the perovskite surface was studied and modeled using DFT (Figure 2A). Here, a MAPbI_3 perovskite slab as well as the PbI_2 and methanaminium iodide (MAI) termination of (001) surfaces with 2×1 periodicity in the x-y plane was used for the adsorption models. For the PbI_2 termination side, the Li^+ of Li-TFSI was prone to fill the absent surface vacancies of MA^+ and interact with surrounding I atoms at the center of the tetrahedral halide cage, leading to strong surface coordination,³⁹ and the $\text{Li}-\text{I}$ bonds exhibit short lengths of 2.75 and 2.80 Å (Figure S6). Meanwhile, the I^+ cation of DIC-PBA coulombically interacted with the surface I^- anion. It showed interatomic distances of 3.59 and 3.53 Å, resulting in weaker interactions compared with those of the above $\text{Li}-\text{I}$ bonds. When the dopant was inverse to the anion side near to perovskite, both dopants of Li-TFSI and DIC-PBA formed $\text{Pb}-\text{F}$ bonds with the perovskite surface. The formation energies (ΔE_f) are defined as $\Delta E_f = E_s - E_z - \sum E_x$ where E_s is the total energy of the perovskite supercell interacting with dopants, E_z is the total energy of the surface of the perovskite supercell, and E_x is the sum of the chemical potential of ions or the total molecular energy that is added or removed from the supercell (Figure 2B). The calculated ΔE_f of Li^+ , DIC^+ , TFSI^- , and PBA^- sides of the dopants adsorbed on the PbI_2 termination of (001) surfaces is -31.92 (Li^+), -29.74 (DIC^+), -34.8 (TFSI^-), and -36.2 (PBA^-) kcal/mol. This indicates that the anion of DIC-PBA preferentially forms on the surface compared with the Li-TFSI dopant and is prone to form forward orientation (F) of dipole (\pm) on the PbI_2 termination surface. For the MAI termination surface, both sides of DIC^+ and PBA^- exhibit weak interactions with the perovskite surface via coulombic interactions and the $\text{N}-\text{H}\cdots\text{F}$ hydrogen bond, respectively,⁴⁰ and they display similar ΔE_f of -16.59 and -15.32 kcal/mol. However, the Li-TFSI cannot maintain a stable geometry of TFSI^- anion orientation with respect to the MAI termination surface and exhibits a dipole parallel to the perovskite surface plane (Figure 2A). This may originate from the stronger electrovalent bond of $\text{Li}-\text{I}$ compared with the hydrogen bond with MA^+ cation, as well as the minor steric hindrance of Li^+ ion, leading it to quickly move to the solid surface. Based on the results of these simulations, the DIC-PBA may display a forward orientation on the perovskite surface, but the Li-TFSI may exhibit a weaker orientation in this direction (Figure 2C). To further confirm the orientation of DIC-PBA, the sum frequency generation (SFG) vibrational spectrum

had been employed for different concentrations of DIC-PBA deposited on the perovskite film. From the SFG spectrum (Figure S7), the $-\text{CH}_3$ symmetric stretching mode (around $2,875 \text{ cm}^{-1}$) and $-\text{CH}_3$ Fermi resonance mode (around $2,960 \text{ cm}^{-1}$) were visible in all the samples of DIC-PBA (different concentrations) deposited on perovskite film.⁴¹ Specifically, the intensity of $-\text{CH}_3$ became lower with the increasing of molecule concentrations, which indicated that the $-\text{CH}_3$ group (DIC^+ cation) was away from the perovskite surface when the concentrations of molecule increased. It further confirmed the weaker interactions of DIC^+ cation compared with the PBA^- anion, which formed a forward (\pm) arrange on the perovskite surface.

The electronic coupling of differently oriented DIC-PBA on the perovskite (both MAI and PbI_2 termination) is visually depicted in an isosurface plot of the charge density difference ($\Delta\rho$); in the PbI_2 termination model (Figure 2H), a strong electron depletion ($\Delta\rho < 0$, negative) appearing around the I atoms of the F-oriented DIC-PBA surface is inverse to the electron accumulation ($\Delta\rho > 0$, positive) around the dopant molecule where it is in contact with the perovskite surface. This implied that the electron transfer is from perovskite to the PBA^- anion group and then to the DIC^+ cation side. However, the electron was localized at the interface between perovskite and the DIC^+ cation when the DIC-PBA dopant inverted to R-orientation, and the same was regularly observed on the MAI termination surface (Figures 2I and S8). To determine the influence of the surface electronic coupling on the E_{Fq} changing patently, the density of states (DOS) employed Pb-dimer defect as the shifting sign is further studied. Figures 2D and 2F described the DOS of both pristine perovskite and R/F-oriented DIC-PBA on perovskite. For the bare perovskite surface, the Fermi level is not located at the valance band edge due to the increased surface electron concentration via the defect-induced n-doping,^{42,43} which is beneficial for observing the E_{Fq} shifting under the R/F-oriented surface dipole. For the perovskite based on F-oriented DIC-PBA, the Fermi level shifts about 0.07 eV toward the valance band edge, indicating that the surface perovskite is prone to convert to a p-type semiconductor due to the as-discussed loss of a surface electron via the molecular charge transfer (Figure 2E). Inversely, the Fermi level shifts toward the conduction band edge ($\Delta E_{\text{Fq}} = 0.38 \text{ eV}$), implying that the perovskite effectively becomes more n-type via the R-oriented dipole (Figure 2G), which may originate from the DIC^+ cation-induced charge localization. These results indicate that the surface R/F-oriented dipole may lead to surface doping via electron transfer and the formation of a p-n homo-junction within the perovskite film to reinforce build in field (E_{bi}) and facilitate the dissociation of photoexcited holes and electrons. To clarify the surface doping by DIC-PBA and Li-TFSI, UPS was carried out to evaluate the electronic structure at the contact perovskite interface (Figures 2J and 2K). The W_{F} ($\Delta\varphi$) of the perovskite increased from 4.55 to 4.65 eV after Li-TFSI surface modification, which verified the effective p-doping within the perovskite surface and thereby narrowed the distance between valence band (VB) and Fermi level ($D_{\text{VB-EF}}$) from 1.62 to 1.58 eV. This may be attributed to the strongly electrophilic fluorine element and Li^+ cation. When the DIC-PBA was substituted to modify the perovskite surface, the $\Delta\varphi$ was further increased to 4.74 eV, indicating that a heavier p-type doping of the perovskite surface is obtained, which might originate from the more oriented DIC-PBA on perovskite. If both dopants show an F-oriented dipole on the perovskite surface, the total surface dipole moment is primarily composed of two portions after the dopant is deposited on the perovskite surface; the first part depends on the effectiveness of the dipole moment supplied by the molecule itself, and the second dipole moment is provided by the interaction between surface atoms and molecule (S-M). The surface potential change caused by the external dipole induced surface electric fields across the basal plane

according to classical electrostatics, and the alteration of the W_F can be expressed by $\Delta\varphi = -N \left[\frac{\mu_{\perp,M}}{\epsilon_0 k_M} + \frac{\mu_{s-M}}{\epsilon_0 k_{s-M}} \right]$, where $\mu_{\perp,M}$ is the dipole moment perpendicular to the perovskite surface, μ_{s-M} represents the dipole moment caused by the surface atomic interactions, N is the grafting density, and κ and ϵ_0 are the dielectric constant of adsorbate and the permittivity of free space, respectively.^{44,45} Therefore, the $\Delta\varphi$ is dependent on the surface atomic interactions (μ_{s-M}) and the magnitude and direction of the molecular dipole moment toward the perovskite surface ($\mu_{\perp,M}$). As discussed, both the Li-TFSI and DIC-PBA dopants would exhibit F-oriented dipole moment on PbI_2 terminated of perovskite. In addition, both of the anions interact with the surface via the Pb–F bond and show a similar bond length (3.11 and 3.15 Å), which means that the second part of the dipole moments (R-oriented) based on Li-TFSI and DIC-PBA is similar ($\mu_x = qL$, the μ_x is the formed dipole moment, q is the charge, and L is the length of bond). However, the length between the centers of positive and negative charges of DIC-PBA compared with Li-TFSI is larger, being respectively, 1.9 and 5.5 Å, and the dipole moments of DIC-PBA and Li-TFSI are, respectively, 28.17 and 5.77 Debye units. This indicates that the total dipole moment is F-oriented, which is consistent with the p-doping of the perovskite surface when modified by either Li-TFSI or DIC-PBA. Moreover, the higher total surface dipole moment and the F-oriented dipole moment of the DIC-PBA may be the reasons that it can obtain higher $\Delta\varphi$ and a resulting heavier p-doping. It also provides higher external E_{bi} via this band blending, which would result in faster separation of the photogenerated electron-hole pairs (Figure S9). To probe the E_{bi} difference using the different dopants, we employed cross-sectional scanning Kelvin probe microscopy (SKPM) to scan the interfaces of devices of FTO (fluorine-doped tin oxide)/c-TiO₂ (compact TiO₂)/m-TiO₂ (mesoporous TiO₂)/perovskite/PTAA/Au. By applying small bias voltages to the device during the measurements, we could resolve the potential drop distribution across the whole device stack. The local potential drop was determined by the equivalent resistance of different layers and interfaces of the device, which is related to the junction quality.^{46,47} In data treatment, we averaged the potential profiles under various bias voltages and then subtracted the 0-V profile to get the “potential difference” curves to remove the effects of static charges on the cross-sectional surface. Finally, we obtained the electric field distribution across the device stack by numerically calculating derivative of the “potential difference.” As a result, it can be seen from the potential difference (Figure S10C, middle) that the DIC-PBA-based devices exhibit a higher difference between perovskite/PTAA interface, especially under –1 V bias voltages conditions. To compare the interface E_{bi} directly, the electric field difference (Figure S10C, bottom) was further studied; obviously, the interface of perovskite/PTAA employing DIC-PBA exhibited higher built-in field. This cross-sectional SKPM further agreed well with the UPS and DFT results. In addition, the Mott-Schottky curves based on FTO/c-TiO₂/m-TiO₂/perovskite/PTAA and the perovskite modified by Li-TFSI and DIC-PBA were further employed to probe the E_{bi} difference and plotted in Figure 2L, where the x axis intercepts indicate the flat-band potentials (V_{fb}). The V_{fb} of the construction based on DIC-PBA was about 0.06 V higher than that obtained by the Li-TFSI-based sample, which verifies the positive effect of the larger and more oriented dipole moment on the E_{bi} . Generally, the surface E_{bi} is associated with the depletion width (W_d) and expressed by $W_d \sim (\epsilon_r E_{bi}/c)^{1/2}$ in the 3D p-n junction, where the ϵ_r represents the relative permittivity of a semiconductor and c is the doping level.^{48,49} It indicates that larger depletion width is obtained when the perovskite surface is tailored with DIC-PBA, which forms a stronger n-p HOMO-junction to promote the interfacial hole transport and suppress the free-charge trap at the defect sites, compared with Li-TFSI. These experimental and theoretical results taken together reveal the great potential of the DIC-PBA dopant for the fabrication of efficient PSCs.

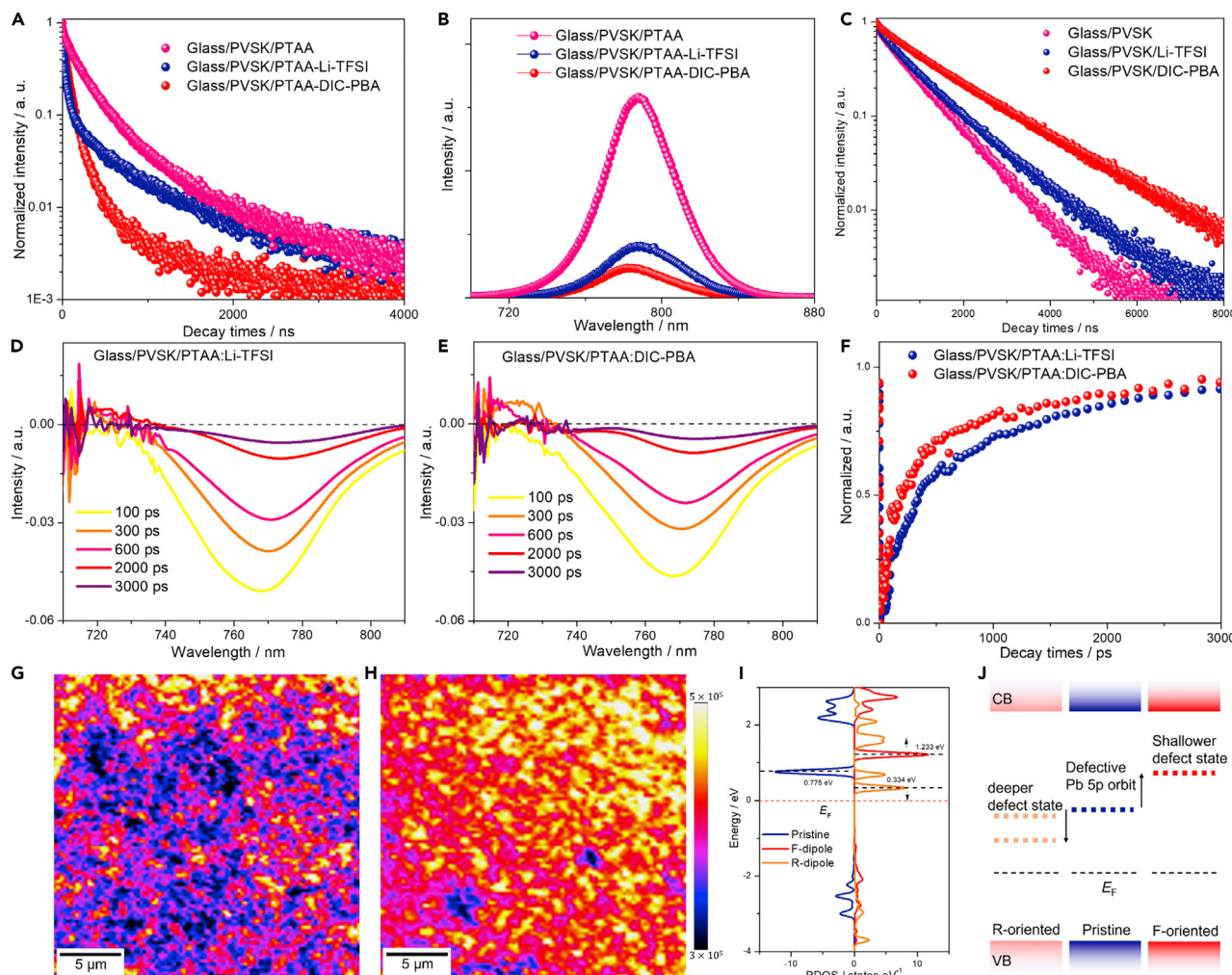


Figure 3. Carrier transfer dynamics

- (A) The TRPL decays of glass/perovskite/PTAA, glass/perovskite/PTAA:Li-TFSI, and glass/perovskite/PTAA:DIC-PBA films.
- (B) The steady-state fluorescence spectra of glass/perovskite/PTAA, glass/perovskite/PTAA:Li-TFSI, and glass/perovskite/PTAA:DIC-PBA films.
- (C) The TRPL decays of glass/perovskite, glass/perovskite/Li-TFSI, and glass/perovskite/DIC-PBA films.
- (D) and (E) represent, respectively, the transient absorption spectra of glass/perovskite/PTAA:Li-TFSI and glass/perovskite/PTAA:DIC-PBA films with a range in the 100–3,000 ps timescale.
- (F) The normalized kinetic traces for photobleaching probed at 770 nm based on glass/perovskite/PTAA:Li-TFSI and glass/perovskite/PTAA:DIC-PBA films.
- (G and H) represent, respectively, the PL mapping of glass/perovskite film modified with Li-TFSI and DIC-PBA dopants.
- (I and J) are, respectively, the PDOS of perovskite Pb-dimer defect interacted with F- and R-oriented dipole and the illustration of defect states shifting under the interaction of differently oriented surface dipoles. The Fermi level was set as zero in this diagram.

To gain insight into the interfacial carrier transport based on the DIC-PBA dopant, time-resolved photoluminescence (TRPL) decay spectroscopy was carried out to study the charge transfer kinetics from the perovskite layer HTL. Figure 3A shows the TRPL spectra of constructions based on glass/perovskite/PTAA, glass/perovskite/PTAA:Li-TFSI, and glass/perovskite/PTAA:DIC-PBA, as well as the delay time fitted by a bi-exponential model with the fast (τ_1) and slow (τ_2) components; the average delay times (τ_{ave}) are calculated by $\tau_{ave} = \sum A_i \tau_i^2 / \sum A_i \tau_i$, where A_i and τ_i represent the decay amplitude and components of the delay time, respectively (detailed delay times are shown in Table S1). For the bare glass/perovskite/PTAA sample, the fast and slow components of PL are 128.6 (τ_1) and 477.2 ns (τ_1), and

the calculated τ_{ave} is 373.8 ns. For PTAA:Li-TFSI-based HTL, the PL sharply decays, and the τ_{ave} decreases to 239.6 ns. When the DIC-PBA dopant was substituted for the Li-TFSI, both τ_1 and τ_2 decreased, respectively, to 21.8 and 132.5 ns with an average decay time of 117.4 ns, which further certified the superior hole injection from the perovskite layer to the HTL compared with Li-TFSI. This probably originates from the heavier surface p-doping via the stronger effective surface dipole moment, which increases the interfacial hole separation, combined with the high intrinsic electrical conductivity of the PTAA. In addition, the steady-state fluorescence spectrum (PL) of samples with the DIC-PBA dopant also displays intense photoluminescent quenching, which agrees well with the faster hole injection observed by TRPL (Figure 3B). Nevertheless, it is observed that the PL peak shifts from 787 to 783 nm when the DIC-PBA is introduced into the PTAA layer, which implies that the dopant may passivate the surface perovskite defects at the contact interface, further hindering surface carrier recombination.

The femtosecond transient absorption (fs-TA) spectra were measured to compare the interfacial carrier dynamics under excited state for the different dopants. Figures 3D and 3E, respectively, are the key ΔOD for a sample based on glass/perovskite/PTAA:Li-TFSI and glass/perovskite/PTAA:DIC-PBA with a series of decay times ranging from 100 to 3,000 ps. It is evident from ΔOD that the positive excited-state absorption (ESA) band observed below 720 nm and a strong negative ground-state bleaching (GSB) band appear at about 770 nm within both Li-TFSI- and DIC-PBA- based samples, which, respectively, originate from the absorption and fluorescent emission of the perovskite. The blue shift of the fluorescent emission peak from ΔOD is consistent with the steady-state PL result (Figure 3B). By comparing with the GSB peak based on Li-TFSI and DIC-PBA at various decay scales, it is evident that the DIC-PBA-based sample displays faster decay of the GSB peaks at 770 nm, which also implies the superior injection of excited-state carriers compared with Li-TFSI. Figure 3F exhibits the temporal evolution of the GSB peaks around 770 nm for the PTAA doped with the Li-TFSI and DIC-PBA, and the quenching of excited-state carriers is fitted by the double exponential function where the ultrafast time decay scale <1,000 ps indicates the effective quenching of interfacial carrier injection and extraction, while the decay in the range from 1 ns to 1 μ s dominates the recombination process of the perovskite absorber itself.^{20,50} To compare the interfacial injection of carriers by using different dopants, the fast component was considered. The sample doped with DIC-PBA exhibited faster decay of the GSB peak at 770 nm and decreased from 108.11 to 56.54 ps, which may be attributed to the heavier p-doping by the surface dipole moment that thereby enhanced the E_{bi} and promoted the interfacial charge injection, as well as the efficient doping of HTL.

To further study the proposed defect passivation effect, the PL and TRPL of glass/perovskite substrate deposited with Li-TFSI and DIC-PBA were measured and are shown in Figures 3C and S11. To realize the trap site change within the perovskite film, only the slow decay process of the bi-exponential decay model was compared. As a result, the recombination lifetime increased from 985.9 ns for the perovskite/Li-TFSI film to 1,392.4 ns for the DIC-PBA-treated perovskite, and both lifetimes were higher than the sample based on glass/perovskite. In addition, the corresponding PL showed stronger PL intensity (Figure S11). Figures 3G and 3H present the visual PL mapping intensity integrated from 675 to 825 nm at the scale of 20 μ m \times 20 μ m, where a higher and more homogeneously distributed PL intensity was observed with DIC-PBA modification. This showed the trap passivation of the perovskite surface via this dopant and finally reduced the density of trap states from 5.86×10^{15}

to $2.98 \times 10^{15} \text{ cm}^{-3}$ (Figure S12) compared with the sample based on Li-TFSI. To probe the passivation mechanism, the detailed partial density of states (PDOS) of perovskite defects interacting with DIC-PBA was described in Figures 3G and 3H. For the bare perovskite model, the I-5p and Pb-6p orbitals contribute to the chlorobenzene (CB) and VB of perovskite, respectively (Figure S13).⁵¹ However, there is a newly observed gap state in the Pb-dimer-based perovskite, which is primarily occupied by the 6p orbitals of the Pb dimer. This gap state always traps the free charge due to the excess hole, and this results in carrier recombination at these defect sites. When the F-oriented DIC-PBA lies on the surface, the p-orbits of the Pb dimer shift about 0.35 eV toward the CB side of the perovskite due to the loss of surface electron via a dipole moment-evoked charge transfer, which is prone to change the deep level trap states within the gap to a shallower one. Inversely, the p-orbitals prefer shifting to the VB side (0.17 eV) when the DIC-PBA is inverse to R-oriented due to the transfer of an electron to the perovskite surface (Figures 3I and 3J). It means that this R-oriented molecular dipole moment will make the trap states become deeper and thus more difficult to de-trap the excited charge carriers even with the extra thermal energy.^{52,53} From the previous discussion, the DIC-PBA possesses a vital dipole moment and prefers forming an F-orientation on the perovskite surface, whereas the Li-TFSI exhibits a weak orientation along this direction. This is probably the dominant reason for the passivation effect observed with the DIC-PBA dopant. Tailoring of the dipole moment and orientation is critical to achieve the surface doping and defect passivation and subsequently interfacial carrier injection and suppressed recombination.

To understand the role of dopants on the photovoltaic properties of PSCs directly, devices based on FTO/c-TiO₂/m-TiO₂/FA_{0.95}MA_{0.05}Pb(I_{0.95}Br_{0.05})₃/PTAA/Au were fabricated, where the PTAA was doped with Li-TFSI and various concentrations of DIC-PBA. Figure 4A represents the cross-section scanning electron microscope (SEM) of devices; it is evident that the thickness of the perovskite film is about 500 nm, and it is only one grain thick due to the large grain size of perovskite (Figure S14), which is favorable to achieve efficient PSCs. Figures 4B and 4C are the J-V characteristics of PSCs based on a range of DIC-PBA doping concentrations. The corresponding statistical results, as well as the detailed parameters of champion PSCs, are shown in Table S2. The parameters of short-circuit current (J_{sc}), fill factor (FF), and V_{oc} are shown to increase with DIC-PBA doping compared with the dopant-free devices. An optimal doping concentration was found at 5% and yielded a PCE of 22.13% with much improved FF and V_{oc} .

Furthermore, the performance of devices based on Li-TFSI and DIC-PBA dopants is compared in Figure 4D, and the detailed data are given in Table S3. The data show that DIC-PBA-doped devices exhibited higher efficiencies essentially due to higher FF and V_{oc} . We believe that this is a result of faster carrier injection at the perovskite/PTAA interface, suppressed interface recombination, and the high conductivity of the HTM. The electric impedance spectroscopy (EIS) shows that the devices based on DIC-PBA exhibit lower reduced series resistance (R_s) and increased shunt resistance (R_{sh}) (Figure S15) compared with Li-TFSI, which is consistent with the observed increases in V_{oc} and FFs. The incident photon-to-current efficiency (IPCE) between 300 and 850 nm was measured to examine the accuracy of the J_{sc} of devices (Figure 4E); the integrated currents of PSCs based on DIC-PBA and Li-TFSI from IPCE achieved 23.15 and 23.08 mA cm⁻², respectively, which were identical to the current obtained from the J-V measurements. In addition, the steady-state efficiency of champion PSCs based on DIC-PBA and Li-TFSI was also measured at a bias voltage of 0.98 and 0.96 V, respectively. As a result, the devices based on DIC-PBA and

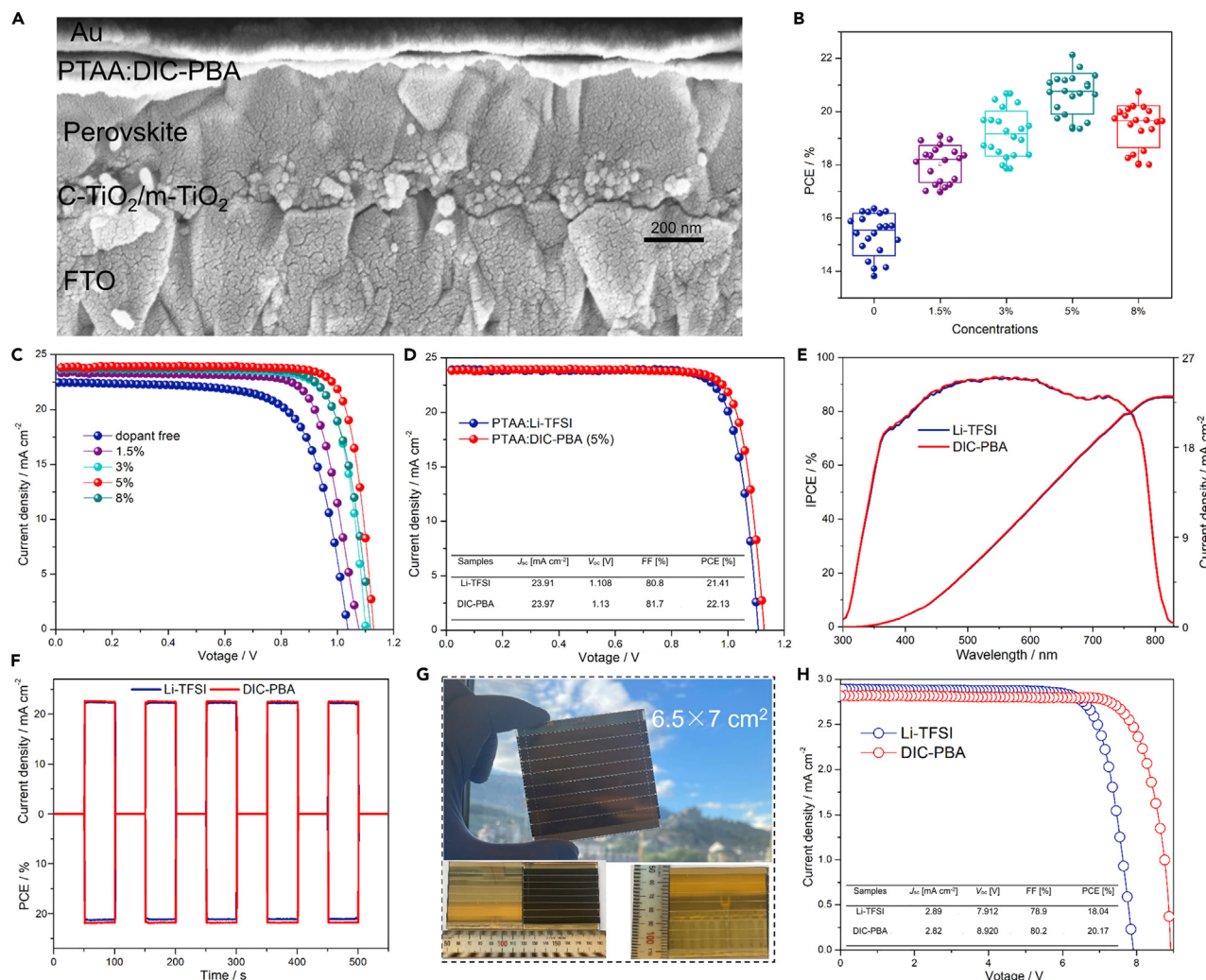


Figure 4. Photovoltaic properties of PSCs

- (A) The cross-section SEM of PSC based on FTO/c-TiO₂/m-TiO₂/perovskite/PTAA:DIC-PBA/Au.
- (B) The statistical distribution of PCEs of PSCs based on DIC-PBA dopant with a series of concentrations.
- (C) The J-V curves of PSCs based on DIC-PBA with various concentrations.
- (D) The J-V curves of champion efficiency of PSCs based on DIC-PBA (5%) and Li-TFSI.
- (E) The IPCE spectra and integrated current densities for PSCs based on DIC-PBA and Li-TFSI/t-BP dopant.
- (F) The steady-state photocurrent and efficiency output at maximum power point and output with 50 s light on/off cycles of devices based on DIC-PBA and Li-TFSI doped PTAA; the output bias voltages are 0.98 and 0.96 V, respectively.
- (G) Photographs of sealed 6.5 × 7 cm² Li-TFSI and DIC-PBA-based solar modules; the active area is 30.24 cm² according to the average of eight separate cells.
- (H) J-V curves of modules based on Li-TFSI and DIC-PBA dopants.

Li-TFSI dopants exhibited, respectively, stabilized PCEs of 21.77% and 21.08% after 50 s cyclic light soaking switch, and both results were extremely close to the efficiency as measured from the J-V curves (Figure 4F).

Besides efficiency, hysteresis performance has also drawn widespread attention for PSCs. The J-V hysteresis is evaluated by the hysteresis index (HI), which is expressed by the formula of $HI = [J_{RS}(0.8 V_{oc}) - J_{FS}(0.8 V_{oc})]/J_{RS}(0.8 V_{oc})$, where $J_{RS}(0.8 V_{oc})$ and $J_{FS}(0.8 V_{oc})$ are, respectively, the photocurrent density at 80% of V_{oc} for the reverse scan and forward scan of J-V curves (Figure S16). The results show that

both devices using the DIC-PBA and Li-TFSI dopants have small HI values of 0.0085 and 0.0229, respectively, indicating that the devices based on the dopant have less hysteresis. This may originate from the faster interfacial carrier injection derived from the oriented dopant dipole moment, which better matches the rapid electron transport within PSCs, as well as from the remission of deep trap states from Pb cation defects via the dipole-derived charge transfer.

After further optimizing the device structure as FTO/c-TiO₂/m-TiO₂/SnO₂/FA_{0.95}-MA_{0.05}Pb(I_{0.95}Br_{0.05})₃/PTAA/Au, the champion efficiency improved to 22.86% with the DIC-PBA dopant with a steady-state efficiency of 22.63% (Figure S17; Table S4), which is the one of the highest efficiency values of PSCs based on PTAA (Table S5). For the Spiro-OMeTAD HTM, the devices based on FTO/c-TiO₂/m-TiO₂/SnO₂/FA_{0.95}MA_{0.05}Pb(I_{0.95}Br_{0.05})₃/Spiro-OMeTAD/Au, the efficiency boosted to 22.73% with 6% doping of DIC-PBA (Figure S18; Tables S6 and S7), indicating the universal effect of the DIC-PBA on the HTM doping.

In terms of the high performance of DIC-PBA-based PSCs, we explored the long-term stabilities of un-encapsulated devices based on Li-TFSI and DIC-PBA dopants under ambient and N₂ conditions. As shown in Figure S19A, DIC-PBA-doped devices display much higher stability under the ambient storage condition (humidity >50%) and retain nearly 90% of their initial PCE after aging for 50 days, whereas Li-TFSI-based PSCs declined to 45% of initial values. This indicates that the dopant will improve the environmental stability of PSCs compared with the Li-TFSI-based sample. Furthermore, when the devices are stored in an N₂-filled glovebox (Figure S19B), the devices can retain 93% and 76% of initial PCE for DIC-PBA- and Li-TFSI-doped HTMs, respectively. The thermal stability is also significant in the real environmental applications. When the devices are heated under 85°C in the N₂-filled glovebox, the performance of the devices based on Li-TFSI decreases dramatically to 71% of initial efficiency after heating for 110 h; however, the devices based on DIC-PBA maintain 97% of the initial efficiency at the same condition (Figure S20). These results imply that the employment of DIC-PBA is not only favorable to improve the environmental stability but also makes the device more intrinsically stable, which is also beneficial for the stability of encapsulated PSCs.

In addition to the performance of PSCs, another issue of importance to commercialization is their large-scale production.⁵⁴ As shown in Figure 4G, guided by these improved physical properties derived from DIC-PBA dopants, we fabricated two modules based on PTAA with different dopants at a size of 6.5 cm × 7 cm. The performance difference between the devices had further increased (Figure 4H). Compared with small devices, the change in the physical properties of perovskite caused by DIC-PBA had a more obvious impact on the performance of the modules. Due to more urgent needs regarding defect passivation and the reduction of the influence of trap states for large-scale devices, the module with DIC-PBA dopant showed better photovoltaic parameters than the reference after the upscaling, especially the V_{oc}. As a result, the perovskite mini-modules reached an efficiency of 20.17% with an active area of 30.24 cm² and an efficiency of 18.38% with an aperture area (geometric FF is 91.1%). Employing with the structure of FTO/c-TiO₂/m-TiO₂/SnO₂/FA_{0.95}MA_{0.05}Pb(I_{0.95}Br_{0.05})₃/PTAA:DIC-PBA/Au, the efficiency of the module improved to 19.13% with an aperture area (33.2 cm²), corresponding to the efficiency of 20.99% with an active area of 30.24 cm² (Figure S17). To the best of our knowledge, this is one of the highest PCEs for all kinds of PSC modules. Therefore, DIC-PBA dopant will play an important role in the commercialization of PSCs in the future.

To gain further insight into the influence of the DIC-PBA dopant on the stability, first, the two-dimensional grazing incidence X-ray diffraction (2D-GIXD) was carried out to observe *in situ* crystalline properties of the devices during aging ([Figures 5A and 5B](#)) under an ambient condition (humidity >50%). When PSCs were aged 40 days, both devices based on DIC-PBA and Li-TFSI exhibited evident signals at $q \approx 10$ and 9 nm^{-1} , which indicate the perovskite reflections of (110) and the PbI_2 reflection, respectively. However, it was different for the Li-TFSI-based sample that showed higher intensity PbI_2 reflections at $q \approx 9 \text{ nm}^{-1}$ and the emergence of the peak of the new reflections at $q \approx 8 \text{ nm}^{-1}$, which is identified as a hydrated perovskite phase.⁵⁵ The results indicate that the Li-TFSI-based devices degenerate more rapidly in the presence of humidity, and that the DIC-PBA dopant helps stabilize the perovskite layer consistent with the almost unchanged perovskite film and devices from the digital photograph ([Figure 5C](#)). This may be attributed to the higher hydrophobicity of DIC-PBA-doped PTAA from the contact angle measurement ([Figure 5F](#)), which is further shown in the photographs that document the changing of perovskite films covered with Li-TFSI and DIC-PBA in humid air (humidity 40%–50%; [Figure S21](#)), as well as to the absence of the use of acetonitrile and *t*-BP with DIC-PBA dopant.

In addition to the negative environmental influence on PSC stability, the migration of ions within the organic-inorganic perovskite lattice is also a non-negligible factor of instability in PSCs, even when they are hermetically sealed.^{27,56} To probe the ionic redistribution within the devices after 40 days of aging, time-of-flight secondary ion mass spectrometry (TOF-SIMS) was employed for devices of FTO/c-TiO₂/m-TiO₂/MAPbBr₃/PTAA:DIC-PBA/Au and FTO/c-TiO₂/m-TiO₂/MAPbBr₃/PTAA:Li-TFSI/Au ([Figures 5D and 5E](#)). The compared TOF-SIMS profiles exhibited that the Li⁺ cation not only distributed within the PTAA layers but also diffused to the TiO₂ layers through the perovskite layers, which agrees well with previous reports.²⁰ However, the DIC⁺ cation, which was tagged as I⁺ ion displayed a concentrated distribution within the PTAA layers and the surface of perovskite, indicating the more immobile DIC-PBA doping at the PTAA layer and the perovskite surface, compared with Li-TFSI. Combined with the previously discussed results, this indicates that both DIC-PBA and Li-TFSI dopants will form an F-oriented dipole moment toward the perovskite surface, which results in an effective p-doping at the contact surface via charge transfer that is favorable for the carrier transport at the perovskite/HTM heterojunction interface. Thus, the migration of Li⁺ cation cannot maintain the stable surface dipole moment; inversely, the DIC-PBA-based devices can remain stable longer, which yield stable band bending at the perovskite surface and retention of fast carrier transport even after aging. The unmoveable dopant ions and durable surface dipole moment supplied by the DIC-PBA may be a vital reason for the improved intrinsic stability under the N₂ atmosphere storage condition and even with 85°C heating. To reveal the reason for the different cation dopant migration behaviors through the perovskite crystal, the migration barriers were explored by DFT calculations and the MAPbBr₃ crystal with a supercell of 2 × 1 along the y axis as the simplified model. As exhibited in [Figure S22](#), the Li⁺ ions migrate to the neighboring MA-site through the tetrahedron cage within both perfect and MA-defective perovskite crystals, since the barriers are 0.29 and 0.15 eV, respectively. The low diffusion barriers imply facile migration of the Li⁺ cation, which agrees with the TOF-SIMS result. When the larger van der Waals radius of K⁺ (1.88 Å) and Cs⁺ (2.16 Å) ions migrate through the tetrahedron cage, the barriers increase to 1.6 eV (MA-defect, 0.8 eV) and 2.3 eV (MA-defect, 0.92 eV), respectively ([Figures 5G and S22](#)). The higher barrier energies indicate that the migration of ions with larger van der Waals radii will be significantly impeded, and this indicates why the DIC⁺ cation is essentially immobile

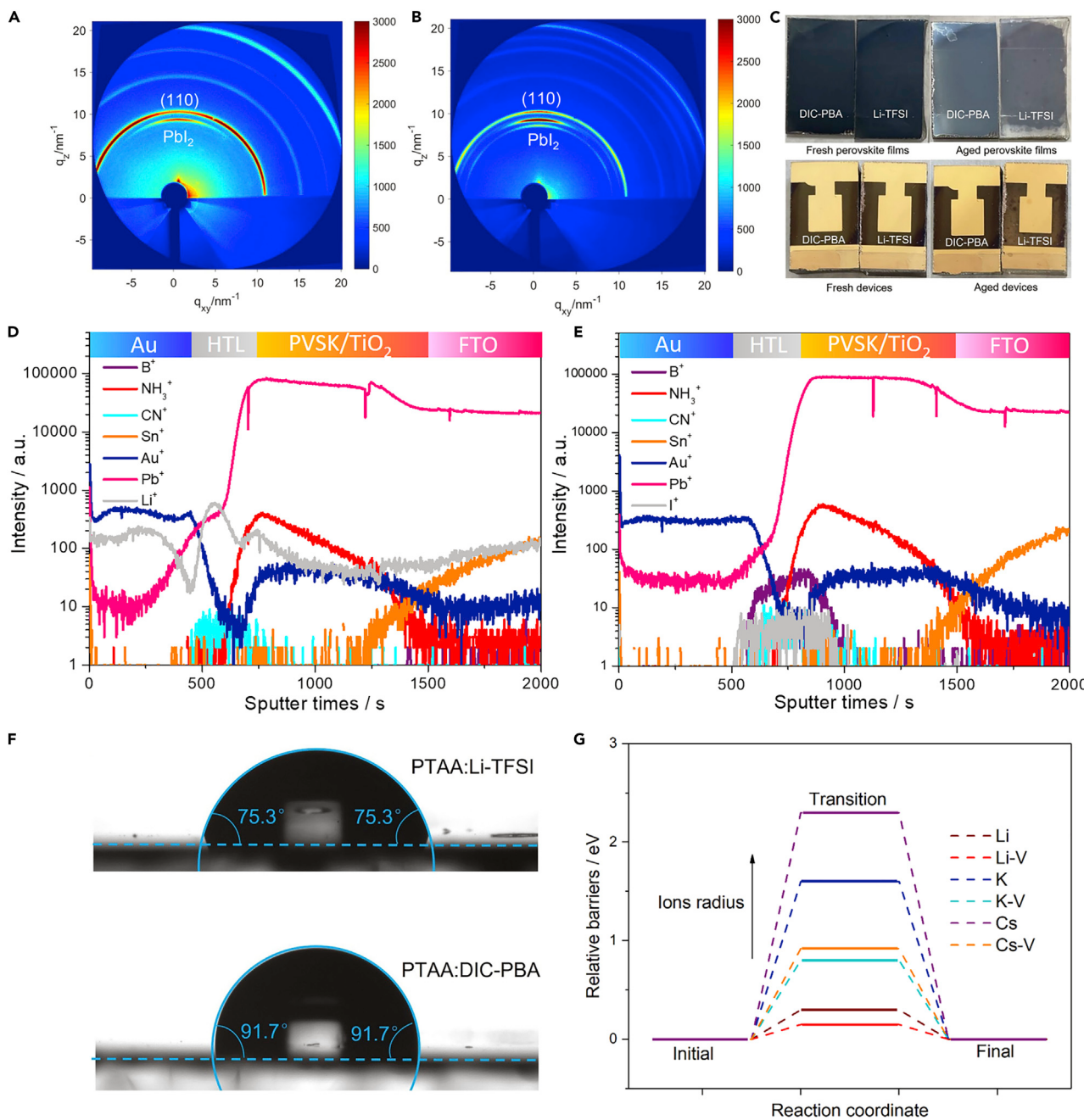


Figure 5. Insight mechanism for remarkable stability

(A and B) (A) and (B) are, respectively, the 2D-GIXRD of the devices based on DIC-PBA and Li-TFSI/t-BP, after dark storage in the ambient atmosphere for 40 days.

(C) The compared initial and aged perovskite film (7 days, the humidity >60%), which is spin coated with DIC-PBA and Li-TFSI and the compared initial and aged devices (18 days, the humidity >60%), which is PTAA doped with DIC-PBA and Li-TFSI.

(D and E) (D) and (E) are, respectively, the TOF-SIMS based on FTO/c-TiO₂/m-TiO₂/MAPbBr₃/PTAA:Li-TFSI/Au and FTO/c-TiO₂/m-TiO₂/MAPbBr₃/PTAA:DIC-PBA/Au dopants after aging for 40 days.

(F) The contact angle of PTAA film based on Li-TFSI and DIC-PBA.

(G) The compared migration barriers of various radius ions to migrate through the MAPbBr₃ perovskite crystal.

in PSCs. These experiments and simulation results further emphasize the role played by dopant ions with large radii on the stability and thus the commercial potential of PSCs. They provide a novel inspiration to design dopants to substitute for the Li-TFSI.

Conclusions

In conclusion, we have demonstrated an efficient and stable organic salt dopant for PTAA, which yielded champion PSCs (small area) with a high efficiency of 22.86% and 19.13% for a module 6.5 cm × 7 cm (aperture area: 33.2 cm²). In addition, the un-encapsulated device retains about 90% of its initial PCE after 1,200 h aging under ambient conditions, compared with 45% for the analogous Li-TFSI/t-BP-based devices. Characterization and analysis showed that the remarkable performance can be attributed to the deep doping of PTAA by DIC-PBA and its strong and specially oriented dipole moment toward the perovskite surface, which forms an effective surface p-doping and trap passivation of Pb-dimers via surface charge transfer, thus averting the carrier recombination at the perovskite/HTM heterojunction. More excitingly, in addition to the higher hydrophobicity of DIC-PBA, the much higher stability can also be ascribed to the intrinsic factor of the stable interfacial dipole due to the much larger van der Waals radius of the DIC⁺ cation compared with the Li⁺ cation. Furthermore, considering the dipole moment of the dopant and its interfacial orientation on the perovskite surface, custom HTM dopant design will play a critical role in the development of large-scale commercially viable PSCs.

EXPERIMENTAL PROCEDURES

Resource availability

Lead contact

Further information and requests for resources and materials should be directed to and will be fulfilled by the lead contact, Mohammad Khaja Nazeeruddin (mdkhaja.nazeeruddin@epfl.ch).

Materials availability

This study did not generate new unique reagents.

Data and code availability

This study did not generate any datasets.

Materials

FAI (99.99%), MABr (99.99%), PbI₂ (99.99%), PbBr₂ (99.99%), 18NR-T, Li-TFSI, t-BP, Spiro-OMeTAD, and PTAA (P226, Mn: 10,800 g/mol, Mw: 210,000 g/mol, solubility: ~120 mg/mL in TL at room temperature) were purchased from Xi'an Polymer Light Technology. The N, N-dimethylformamide (DMF), dimethyl sulfoxide (DMSO), ethanol, CB, acetonitrile, and tin(IV) chloride pentahydrate were obtained from Sigma-Aldrich. All other solvents and chemicals were obtained from commercial sources and used as received without further purification. The c-TiO₂ precursor solution was prepared as follows: 369 μL of titanium isopropoxide was added into 2.53 mL of ethanol, and 35 μL of 2M HCl solution was added into 2.53 mL of ethanol in another vial simultaneously. The m-TiO₂ solution was obtained by diluting the 18NR-T in ethanol with a ratio of 1:7. For the SnO₂ solution, 12 μL SnCl₄ solution was dissolved in 988 μL of deionized water. For the preparation of the perovskite precursor solution, the FAI (228.76 mg), PbI₂ (613.13 mg), MABr (7.84 mg), PbBr₂ (25.69 mg), and MACl (33 mg) were dissolved in 1 mL of a mixed solution of DMF/DMSO (8:1 v/v). The control PTAA solution was prepared by dissolving 15 mg of PTAA in 1 mL of TL, in which 7.5 μL Li-bis(trifluoromethanesulfonyl) imide

(Li-TFSI)/acetonitrile (170 mg/1 mL) and 7.5 μ L t-BP were added. The PTAA (15 mg) and DIC-PBA were dissolved into 1 mL TL and mixed by desired DIC-PBA/PTAA ratios ranging from 1.5% to 8% (mole ratio with respect to the repeat unit mass). The Spiro-OMeTAD solution was prepared by dissolving 72.3 mg Spiro-OMeTAD, 28.8 μ L of t-BP, and 17.5 μ L of (Li-TFSI) solution (520 mg Li-TFSI in 1 mL acetonitrile) in 1 mL CB. For DIC-PBA doped solutions, the Spiro-OMeTAD (72.3 mg) and DIC-PBA were dissolved into 1 mL CB and mixed by desired DIC-PBA/Spiro-OMeTAD with a range of mole ratios. All the solutions were passed through a 0.22- μ m filter before use, except the m-TiO₂ solution.

Fabrication

For the small area devices, all component layers were prepared in an N₂-filled glove box. The precleaned, FTO-coated glass substrates were treated with UV-ozone 20 min before device fabrication. The c-TiO₂ solution was spin coated at 4,000 rpm for 50 s, followed by heating at 150°C for 15 min, and then the c-TiO₂ films were gradually heated to 500°C and baked at this temperature for 30 min. The m-TiO₂ layers were deposited on FTO/c-TiO₂ substrates via spin coating m-TiO₂ precursor solution at 5,000 rpm for 30 s; the layers were then dried at 125°C for 10 min and sintered at 500°C for 30 min; the perovskite solution was spin coated in a two-step program at 1,000 and 4,000 rpm for 10 and 30 s, respectively. During the second step, 1 mL diethyl ether was poured on the spinning substrate 20 s before the end of the program, followed by heating at 150°C for 20 min. Afterward, the PTAA/Spiro-OMeTAD solution was deposited on the perovskite layers by spin coating at 3,000 rpm for 30 s. Finally, the Au electrode was thermally evaporated on the PTAA/Spiro-OMeTAD-coated film, and the active area of each device was 0.09 cm². For the SnO₂-based devices, the SnO₂ solution was spin coated on m-TiO₂ at 3,000 rpm for 30 s; all other processes were similar to the c-TiO₂/m-TiO₂-based devices.

The module was composed of eight-strip cells connected in series using P1-, P2-, and P3-type interconnects. The laser structuring of all three scribes (P1, P2, P3) was made with the same near infrared 1,064 nm, 20-W laser (Trotec). For fabrication of solar modules, 6.5 cm × 7 cm FTO substrates were patterned by a laser with a scribing width of 40 μ m (speed 300 mm/s, frequency 65 kHz, pulse duration: 120 ns, power 60%). To form a 20–25-nm-thick TiO₂ blocking layer, diluted TAA solution (Sigma-Aldrich) in ethanol (0.2 mL of TAA in 6 mL of anhydrous ethanol) was sprayed at 450°C. The m-TiO₂ was coated on the substrate by spin coating at a speed of 3,000 rpm for 30 s from a commercially available TiO₂ in ethanol (10:1, weight ratio); the substrate was immediately dried on a hotplate at 80°C, and the substrates were then sintered at 500°C for 20 min. The fabrication of the perovskite film and PTAA layer are identical to the preparation of small area devices, except that the anti-solvent for perovskite was changed to 1 mL of CB. Next, c-TiO₂/m-TiO₂/perovskite/PTAA layers were scribed by a laser with a scribing width of 400 μ m (multiple parallel scribes with 50- μ m spacing, speed 1,000 mm/s, pulse duration 120 ns, frequency 65 kHz, and power 15%). Finally, a gold electrode was deposited by thermal evaporation, and gold layers were scribed by a laser with a scribing width of 50 μ m (speed 1,000 mm/s, pulse duration 120 ns, frequency 65 kHz, and power 15%). For the SnO₂-based devices, the SnO₂ solution was spin coated on m-TiO₂ at 3,000 rpm for 30 s; all other processes were similar to the c-TiO₂/m-TiO₂-based device.

Characterization

The ultraviolet photoelectron spectroscopy (UPS) measurements were performed by AXIS ULTRA DLD with a He I monochromator (21.22 eV); the HOMO level was given

by: $E_{\text{HOMO}} = -(\varphi + E_{\text{onset}})$, the φ is the W_F of the film. The morphologies of the perovskite films were observed by SEM (JEOL JSM-7600F). The steady-state PL spectra were performed using a HITACHI (model F-4600) spectrophotometer, and the exciting wavelength was 460 nm. The TRPL spectra were measured at room temperature using a time-correlated single-photon counting (TCSPC) technique with an excitation wavelength of 474 nm. An emission wavelength of 785 nm was used for the measurement. The fs-TA spectra were performed using a femtosecond regenerative amplified Ti: sapphire laser system (Spectra-Physics, Spitfire-Pro) and an automated data acquisition system (ultrafast systems, Helios Fire). The emission wavelength was about 770 nm, and the delay curves were fitted by double exponential functions. The J-V curves of the PSCs were measured by using an electrochemical workstation (CHI 660E, Shanghai Chenhua) under AM 1.5G simulated solar light (100 mW cm^{-2}) (CHF-XM-500W, Trusttech, Beijing, China). The incident light intensity was calibrated with a standard Si solar cell. The EIS of the PSCs was recorded by an electrochemical workstation (CHI 660E, Shanghai Chenhua, China) with a bias potential of 0.8 V. The incident photon-to-electron conversion efficiency (IPCE) spectra were performed by using a commercial setup (QTest Station 2000 IPCE Measurement System, CROWNTECH, USA). The contact angles were measured by using a commercial setup (HHUAVE A23-605L). 2D-GIXD images were conducted at BSRF 1W1A. The ion distribution of perovskite device was measured by TOF-SIMS (TOF.SIMS 5, ION-TOF GmbH, Germany).⁵⁶ The SFG spectrometer is a commercial setup built by Ekspla based on Nd:YAG picosecond laser system. A copropagating configuration is exploited. The visible light pulse is of 532 nm, and the infrared (IR) pulse is adjustable ranging from 1,000 to 4,000 cm^{-1} . The incident angle is 60° for the visible beam and 55° for the IR beam. The energy of the visible and IR beams is generally less than 200 μJ , and the photodamage effect is negligible for the studied samples. The polarization combination is typically SSP (s-SFG, s-visible, and p-infrared) during the experiment. For SFG measurements, the two lights directly shine on the interface of interest, spatially and temporally overlapped, and the so-generated sum frequency light is directed to the detector through a series of filters and polarization analyzer. SKPM measurements were taken on a home-built SKPM system based on Vecco D5000 AFM located in an Ar-filled glovebox with water and oxygen levels lower than 0.1 ppm. SKPM scans in tapping mode; it measures the electrostatic signal by constantly nullifying the coulomb force between the AFM probe (nanosensor PPP-EFM) and the sample. Topography and potential images were acquired simultaneously. The mapping has a 30 nm spatial resolution and a 10-mV electrical resolution. We apply bias voltages (-0.5 and -1 V) for SKPM in dark conditions.

DFT calculations

The calculation of geometry optimization was performed by the Gaussian 09W program using the B3LYP exchange-correlation functional⁵⁷, and the Multiwfnn program further calculated the van der Waals radius.⁵⁸ Other geometry optimization and interactions were performed in the DFT framework and carried out by the CASTEP package⁵⁹ with a generalized gradient approximation-Perdew Burke Ernzerh (GGA-PBE) exchange-correlation functional.⁶⁰ The self-consistent field (SCF) convergence criterion of $1 \times 10^{-6} \text{ eV}$ was adopted to the geometry optimization, and the total energy convergence tolerance and force tolerance were set to be $1 \times 10^{-5} \text{ eV}$, $2 \times 10^{-2} \text{ eV } \text{\AA}^{-1}$, respectively. For the perovskite slabs, to simplify the calculations, the $\text{CH}_3\text{NH}_3\text{PbI}_3$ (MAPbI₃) perovskite with stable (001) surface⁶¹ was employed as a slab for the calculation of trap states. The 20 Å vacuum was added on top of the surface of the slabs to minimize the interaction with a Monkhorst-Pack k-point mesh of $2 \times 2 \times 1$, and the cutoff energy was set as 600 eV. The formation energies (ΔE_f) are defined as $\Delta E_f = E_s - E_z - \sum E_x$, where E_s means

the total energy of the perovskite supercell interacting with the molecule, E_z is the total energy of the surface of the perovskite supercell, and E_x is the sum of the chemical potential of ions or total energy of molecule that are added or removed from the supercell. The charge density difference was carried out by the Vienna ab-initio simulation package (VASP) program^{62,63} and defined as $\Delta\rho = \rho_{\text{final}} - \rho_{\text{initial}} - \rho_i$, where ρ_{final} , ρ_{initial} , and ρ_i denote the charge density of the optimized adsorbed slabs, the corresponding separated slab without the adsorbed molecules, and the molecules itself, respectively.

SUPPLEMENTAL INFORMATION

Supplemental information can be found online at <https://doi.org/10.1016/j.joule.2022.05.012>.

ACKNOWLEDGMENTS

We are grateful to the National Natural Science Foundation of China (grant no. 22175029), the Fundamental Research Funds for the Central Universities of China (grant nos. ZYGX2019Z007, Y030202059018023, and Y0301902610100214), the National Key Research and Development Program of China (grant no. 2017YFB0702802), and Sichuan Science and Technology Program (grant no. 2020YJ0029) for financial support. This publication was made possible by NPRP grant no. NPRP11S-1231-170150 from the Qatar National Research Fund (a member of Qatar Foundation). The authors extend their appreciation to the Deputyship for Research & Innovation, Ministry of Education in Saudi Arabia for funding this research work through the project number 526. This work was authored in part by the National Renewable Energy Laboratory (NREL), operated by Alliance for Sustainable Energy for the US Department of Energy (DOE) under contract no. DE-AC36-08GO28308. Funding for work at NREL was provided by DOE Office of Energy Efficiency and Renewable Energy Solar Energy Technologies Office under the De-risking Halide Perovskite Solar Cells Program. This work was supported by the VALAIS ENERGY DEMONSTRATORS FUND, and the authors extend their appreciation to the Deputyship for Research & Innovation, Ministry of Education in Saudi Arabia for funding this research work through the project number 526. We also thank the Academic Support Plan for doctoral students of UESTC for the financial support and thank the Beijing Synchrotron Radiation Facility (BSRF) 1W1A for 2D-GIXD measurements.

AUTHOR CONTRIBUTIONS

J.X. and Y.Z. fabricated the devices. H.Y. and J.L. helped prepare the 2D-GIXD sample and measurement. J.X., X.Y., and Y.S. performed and discussed the DFT calculation. N.I.D.K. performed the UPS measurement. J.Z. performed the PL mapping measurement. H.L. performed the SFG measurement. C.X., M.C., and J.M.L. performed the SKPM measurement. J.X. wrote the first draft of the manuscript. J.C., A.M.A., K.G.B., C.J., and M.K.N. revised the manuscript. All authors contributed to the discussion and commented on the manuscript. C.J. and M.K.N. conceived and supervised the project.

DECLARATION OF INTERESTS

The authors declare no competing interests.

Received: August 2, 2021

Revised: September 24, 2021

Accepted: May 19, 2022

Published: June 14, 2022

REFERENCES

1. Kojima, A., Teshima, K., Shirai, Y., and Miyasaka, T. (2009). Organometal halide perovskites as visible-light sensitizers for photovoltaic cells. *J. Am. Chem. Soc.* 131, 6050–6051.
2. Im, J.H., Lee, C.R., Lee, J.W., Park, S.W., and Park, N.G. (2011). 6.5% efficient perovskite quantum-dot-sensitized solar cell. *Nanoscale* 3, 4088–4093.
3. Heo, J.H., Im, S.H., Noh, J.H., Mandal, T.N., Lim, C.S., Chang, J.A., Lee, Y.H., Kim, H.J., Sarkar, A., Nazeeruddin, M.K., et al. (2013). Efficient inorganic-organic hybrid heterojunction solar cells containing perovskite compound and polymeric hole conductors. *Nat. Photonics* 5, 486–491.
4. Burschka, J., Pellet, N., Moon, S.J., Humphry-Baker, R., Gao, P., Nazeeruddin, M.K., and Grätzel, M. (2013). Sequential deposition as a route to high-performance perovskite-sensitized solar cells. *Nature* 499, 316–319.
5. Cruz, D., Garcia Cerrillo, J., Kumru, B., Li, N., Dario Perea, J., Schmidt, B.V.K.J., Lauermann, I., Brabec, C.J., and Antonietti, M. (2019). Influence of thiazole-modified carbon nitride nanosheets with feasible electronic properties on inverted perovskite solar cells. *J. Am. Chem. Soc.* 141, 12322–12328.
6. Kim, M., Motti, S.G., Sorrentino, R., and Petrozza, A. (2018). Enhanced solar cell stability by hygroscopic polymer passivation of metal halide perovskite thin film. *Energy Environ. Sci.* 11, 2609–2619.
7. Hou, Y., Du, X., Scheiner, S., McMeekin, D.P., Wang, Z., Li, N., Killian, M.S., Chen, H., Richter, M., Levchuk, I., et al. (2017). A generic interface to reduce the efficiency-stability-cost gap of perovskite solar cells. *Science* 358, 1192–1197.
8. Tan, B., Raga, S.R., Chesman, A.S.R., Füller, S.O., Zheng, F., McMeekin, D.P., Jiang, L., Mao, W., Lin, X., Wen, X., et al. (2019). LiTFSI-free spiro-OMeTAD-based perovskite solar cells with power conversion efficiencies exceeding 19%. *Adv. Energy Mater.* 9, 1901519.
9. Cao, Y., Li, Y., Morrissey, T., Lam, B., Patrick, B.O., Dvorak, D.J., Xia, Z., Kelly, T.L., and Berlinguet, C.P. (2019). Dopant-free molecular hole transport material that mediates a 20% power conversion efficiency in a perovskite solar cell. *Energy Environ. Sci.* 12, 3502–3507.
10. Yoo, J.J., Wieghold, S., Sponseller, M.C., Chua, M.R., Bertram, S.N., Hartono, N.T.P., Tresback, J.S., Hansen, E.C., Correa-Baena, J., Bulović, V., et al. (2019). An interface stabilized perovskite solar cell with high stabilized efficiency and low voltage loss. *Energy Environ. Sci.* 12, 2192–2199.
11. Gao, X.X., Luo, W., Zhang, Y., Hu, R., Zhang, B., Züttel, A., Feng, Y., and Nazeeruddin, M.K. (2020). Stable and high-efficiency methylammonium-free perovskite solar cells. *Adv. Mater.* 32, e1905502.
12. Kim, M., Kim, G., Lee, T.K., Choi, I.W., Choi, H.W., Jo, Y., Yoon, Y.J., Kim, J.W., Lee, J., Huh, D., et al. (2019). Methylammonium chloride induces intermediate phase stabilization for efficient perovskite solar cells. *Joule* 3, 2179–2192.
13. Jeong, J., Kim, M., Seo, J., Lu, H., Ahlawat, P., Mishra, A., Yang, Y., Hope, M.A., Eickemeyer, F.T., Kim, M., et al. (2021). Pseudo-halide anion engineering for α -FAPbI₃ perovskite solar cells. *Nature* 592, 381–385.
14. National Renewable Energy Laboratory. Best research cell efficiency. <https://www.nrel.gov/pv/cell-efficiency.html>.
15. Kong, J., Shin, Y., Röhr, J.A., Wang, H., Meng, J., Wu, Y., Katzenberg, A., Kim, G., Kim, D.Y., Li, T.D., et al. (2021). CO₂ doping of organic interlayers for perovskite solar cells. *Nature* 594, 51–56.
16. Song, S., Park, E.Y., Ma, B.S., Kim, D.J., Park, H.H., Kim, Y.Y., Shin, S.S., Jeon, N.J., Kim, T., and Seo, J. (2021). Selective defect passivation and topographical control of 4-dimethylaminopyridine at grain boundary for efficient and stable planar perovskite solar cells. *Adv. Energy Mater.* 11, 2003382.
17. Caliò, L., Salado, M., Kazim, S., and Ahmad, S. (2018). A generic route of hydrophobic doping in hole transporting material to increase longevity of perovskite solar cells. *Joule* 2, 1800–1815.
18. Wang, K., Liu, X., Huang, R., Wu, C., Yang, D., Hu, X., Jiang, X., Duchamp, J.C., Dorn, H., and Priya, S. (2019). Nonionic Sc₃N@C80 dopant for efficient and stable halide perovskite photovoltaics. *ACS Energy Lett.* 4, 1852–1861.
19. Xu, B., Zhu, Z., Zhang, J., Liu, H., Chueh, C., Li, X., and Jen, A.K.-Y. (2017). 4-tert-Butylpyridine free organic hole transporting materials for stable and efficient planar perovskite solar cells. *Adv. Energy Mater.* 7, 1700683.
20. Luo, J., Xia, J., Yang, H., Chen, L., Wan, Z., Han, F., Malik, H.A., Zhu, X., and Jia, C. (2018). Toward high-efficiency, hysteresis-less, stable perovskite solar cells: unusual doping of a hole-transporting material using a fluorine-containing hydrophobic Lewis acid. *Energy Environ. Sci.* 11, 2035–2045.
21. Zhang, J., Zhang, T., Jiang, L., Bach, U., and Cheng, Y. (2018). 4-tert-Butylpyridine free hole transport materials for efficient perovskite solar cells: a new strategy to enhance the environmental and thermal stability. *ACS Energy Lett.* 3, 1677–1682.
22. Li, Z., Tinkham, J., Schulz, P., Yang, M., Kim, D.H., Berry, J., Sellinger, A., and Zhu, K. (2017). Acid additives enhancing the conductivity of spiro-OMeTAD toward high-efficiency and hysteresis-less planar perovskite solar cells. *Adv. Energy Mater.* 7, 1601451.
23. Jiang, L., Wang, Z., Li, M., Li, C., Fang, P., and Liao, L. (2019). Flower-like MoS₂ nanocrystals: a powerful sorbent of Li⁺ in the spiro-OMeTAD layer for highly efficient and stable perovskite solar cells. *J. Mater. Chem. A* 7, 3655–3663.
24. Jeon, I., Ueno, H., Seo, S., Aitola, K., Nishikubo, R., Saeki, A., Okada, H., Boschloo, G., Maruyama, S., and Matsuo, Y. (2018). Lithium-ion endohedral fullerene (Li⁺@C₆₀) dopants in stable perovskite solar cells induce instant doping and anti-oxidation. *Angew. Chem. Int. Ed. Engl.* 57, 4607–4611.
25. Dong, Y., Zhang, J., Yang, Y., Qiu, L., Xia, D., Lin, K., Wang, J., Fan, X., and Fan, R. (2019). Self-assembly of hybrid oxidant POM@Cu-BTC for enhanced efficiency and long-term stability of perovskite solar cells. *Angew. Chem. Int. Ed. Engl.* 58, 17610–17615.
26. Li, M., Xia, D., Yang, Y., Du, X., Dong, G., Jiang, A., and Fan, R. (2018). Doping of [In₂(phen)₃Cl₆]·CH₃CN·2H₂O indium-based metal-organic framework into hole transport layer for enhancing perovskite solar cell efficiencies. *Adv. Energy Mater.* 8, 1702052.
27. Ran, C., Xu, J., Gao, W., Huang, C., and Dou, S. (2018). Defects in metal triiodide perovskite materials towards high-performance solar cells: origin, impact, characterization, and engineering. *Chem. Soc. Rev.* 47, 4581–4610.
28. Xiao, Z., Yuan, Y., Shao, Y., Wang, Q., Dong, Q., Bi, C., Sharma, P., Gruber, A., and Huang, J. (2015). Giant switchable photovoltaic effect in organometal trihalide perovskite devices. *Nat. Mater.* 14, 193–198.
29. Li, Z., Xiao, C., Yang, Y., Harvey, S.P., Kim, D.H., Christians, J.A., Yang, M., Schulz, P., Nanayakkara, S.U., Jiang, C., et al. (2017). Extrinsic ion migration in perovskite solar cells. *Energy Environ. Sci.* 10, 1234–1242.
30. Ansari, F., Shirzadi, E., Salavati-Niasari, M., LaGrange, T., Nonomura, K., Yum, J.H., Sivila, K., Zakeeruddin, S.M., Nazeeruddin, M.K., Grätzel, M., et al. (2020). Passivation mechanism exploiting surface dipoles affords high-performance perovskite solar cells. *J. Am. Chem. Soc.* 142, 11428–11433.
31. Kim, H., Pei, M., Lee, Y., Sutanto, A.A., Paek, S., Queloz, V.I.E., Huckaba, A.J., Cho, K.T., Yun, H.J., Yang, H., et al. (2020). Self-crystallized multifunctional 2D perovskite for efficient and stable perovskite solar cells. *Adv. Funct. Mater.* 30, 1910620.
32. Xia, J., Luo, J., Yang, H., Zhao, F., Wan, Z., Malik, H.A., Shi, Y., Han, K., Yao, X., and Jia, C. (2020). Vertical phase separated cesium fluoride doping organic electron transport layer: A facile and efficient “bridge” linked heterojunction for perovskite solar cells. *Adv. Funct. Mater.* 30, 2001418.
33. Wang, B., Li, H., Dai, Q., Zhang, M., Zou, Z., Brédas, J.L., and Lin, Z. (2021). Robust molecular dipole-enabled defect passivation and control of energy-level alignment for high-efficiency perovskite solar cells. *Angew. Chem. Int. Ed. Engl.* 60, 17664–17670.
34. Kahn, A. (2016). Fermi level, work function and vacuum level. *Mater. Horiz.* 3, 7–10.
35. Tang, C.G., Ang, M.C.Y., Choo, K.K., Keerthi, V., Tan, J.K., Syafiqah, M.N., Kugler, T., Burroughes, J.H., Png, R.Q., Chua, L.L., et al. (2016). Doped polymer semiconductors with ultrahigh and ultralow work functions for ohmic contacts. *Nature* 539, 536–540.
36. Shao, Y., Yuan, Y., and Huang, J. (2016). Correlation of energy disorder and open-circuit voltage in hybrid perovskite solar cells. *Nat. Energy* 1, 15001.

37. Xia, J., Luo, J., Yang, H., Sun, C., Wan, Z., Malik, H.A., Zhang, H., Shi, Y., and Jia, C. (2019). Ionic selective contact controls the charge accumulation for efficient and intrinsic stable planar homo-junction perovskite solar cells. *Nano Energy* 66, 104098.
38. Gaulding, E.A., Hao, J., Kang, H.S., Miller, E.M., Haberreutinger, S.N., Zhao, Q., Hazarika, A., Sercel, P.C., Luther, J.M., and Blackburn, J.L. (2019). Conductivity tuning via doping with electron donating and withdrawing molecules in perovskite CsPbI_3 nanocrystal films. *Adv. Mater.* 31, e1902250.
39. You, S., Wang, H., Bi, S., Zhou, J., Qin, L., Qiu, X., Zhao, Z., Xu, Y., Zhang, Y., Shi, X., et al. (2018). A biopolymer heparin sodium interlayer anchoring TiO_2 and MAPbI_3 enhances trap passivation and device stability in perovskite solar cells. *Adv. Mater.* 30, e1706924.
40. Li, N., Tao, S., Chen, Y., Niu, X., Onwudinanti, C.K., Hu, C., Oiu, Z., Xu, Z., Zheng, G., Wang, L., et al. (2019). Cation and anion immobilization through chemical bonding enhancement with fluorides for stable halide perovskite solar cells. *Nat. Energy* 4, 408–415.
41. Zhang, M., Chen, Q., Xue, R., Zhan, Y., Wang, C., Lai, J., Yang, J., Lin, H., Yao, J., Li, Y., et al. (2019). Reconfiguration of interfacial energy band structure for high-performance inverted structure perovskite solar cells. *Nat. Commun.* 10, 4593.
42. Peng, W., Yin, J., Ho, K.T., Ouellette, O., De Bastiani, M., Murali, B., El Tall, O., Shen, C., Miao, X., Pan, J., et al. (2017). Ultralow self-doping in two-dimensional hybrid perovskite single crystals. *Nano Lett.* 17, 4759–4767.
43. Ou, Q., Zhang, Y., Wang, Z., Yuwono, J.A., Wang, R., Dai, Z., Li, W., Zheng, C., Xu, Z.Q., Qi, X., et al. (2018). Strong depletion in hybrid perovskite p-n junctions induced by local electronic doping. *Adv. Mater.* 30, e1705792.
44. Boer, B. de, Hadipour, A., Mandoc, M.M., van Woudenberg, T.V., and Blom, P.W.M. (2005). Tuning of metal work functions with self-assembled monolayers. *Adv. Mater.* 17, 621–625.
45. Ali, F., Roldán-Carmona, C., Sohail, M., and Nazeeruddin, M.K. (2020). Applications of self-assembled monolayers for perovskite solar cells interface engineering to address efficiency and stability. *Adv. Energy Mater.* 10, 2002989.
46. Xiao, C., Wang, C., Ke, W., Gorman, B.P., Ye, J., Jiang, C.S., Yan, Y., and Al-Jassim, M.M. (2017). Junction quality of SnO_2 -based perovskite solar cells investigated by nanometer-scale electrical potential profiling. *ACS Appl. Mater. Interfaces* 9, 38373–38380.
47. Xiao, C., Zhang, F., Chen, X., Yang, M., Harvey, S.P., Beard, M.C., Berry, J.J., Jiang, C., Al-Jassim, M.M., and Zhu, K. (2021). SMART perovskite growth: Enabling a larger range of process conditions. *ACS Energy Lett.* 6, 650–658.
48. Achoyan, A.S., Yesayan, A.É., Kazaryan, É.M., and Petrosyan, S.G. (2002). Two-dimensional p-n junction under equilibrium conditions. *Semiconductors* 36, 903–907.
49. Yu, H., Kutana, A., and Yakobson, B.I. (2016). Carrier delocalization in two-dimensional coplanar p-n junctions of graphene and metal dichalcogenides. *Nano Lett.* 16, 5032–5036.
50. Tress, W. (2017). Perovskite solar cells on the way to their radiative efficiency limit—insights into a success story of high open-circuit voltage and low recombination. *Adv. Energy Mater.* 7, 1602358.
51. Zhang, J., Chen, R., Wu, Y., Shang, M., Zeng, Z., Zhang, Y., Zhu, Y., and Han, L. (2018). Extrinsic movable ions in MAPbI_3 modulate energy band alignment in perovskite solar cells. *Adv. Energy Mater.* 8, 1701981.
52. Kim, H., Kim, J.S., Heo, J.M., Pei, M., Park, I.H., Liu, Z., Yun, H.J., Park, M.H., Jeong, S.H., Kim, Y.H., et al. (2020). Proton-transfer-induced 3D/2D hybrid perovskites suppress ion migration and reduce luminance overshoot. *Nat. Commun.* 11, 3378.
53. Fu, J., Jamaludin, N.F., Wu, B., Li, M., Solanki, A., Ng, Y.F., Mhaisalkar, S., Huan, C.H.A., and Sum, T.C. (2019). Localized traps limited recombination in lead bromide perovskites. *Adv. Energy Mater.* 9, 1803119.
54. Zhang, Y., Chen, M., Zhou, Y., Li, W., Lee, Y., Kanda, H., Gao, X., Hu, R., Brooks, K.G., Zia, R., et al. (2020). The synergism of DMSO and diethyl ether for highly reproducible and efficient $\text{MA}_0.5\text{FA}_{0.5}\text{PbI}_3$ perovskite solar cells. *Adv. Energy Mater.* 10, 2001300.
55. Hu, Y., Schlipf, J., Wussler, M., Petrus, M.L., Jaegermann, W., Bein, T., Müller-Buschbaum, P., and Docampo, P. (2016). Hybrid perovskite-perovskite heterojunction solar cells. *ACS Nano* 10, 5999–6007.
56. Christians, J.A., Schulz, P., Tinkham, J.S., Schloemer, T.H., Harvey, S.P., de Villers, B.J.T., Sellinger, A., Berry, J.J., and Luther, J.M. (2018). Tailored interfaces of unencapsulated perovskite solar cells for >1000 hour operational stability. *Nat. Energy* 3, 68–74.
57. Frisch, M.J., Trucks, G.W., Schlegel, H.B., Scuseria, G.E., Robb, M.A., Cheeseman, J.R., Montgomery, J.A., Jr., Vreven, T., Kudin, K.N., Burant, J.C., et al. (2009). Gaussian 09 Revision A.02 (Gaussian, Incorp.).
58. Lu, T., and Chen, F. (2012). Multiwfn: a multifunctional wavefunction analyser. *J. Comput. Chem.* 33, 580–592.
59. Clark, S.J., Segall, M.D., Pickard, C.J., Hasnip, P.J., Probert, M.I.J., Refson, K., and Payne, M.C. (2005). First principles methods using CASTEP. *Z. Krist.* 220, 567–570.
60. Perdew, J.P., Burke, K., and Ernzerhof, M. (1996). Generalized gradient approximation made simple. *Phys. Rev. Lett.* 77, 3865–3868.
61. Liu, L., Fang, W.H., Long, R., and Prezhdo, O.V. (2018). Lewis base passivation of hybrid halide perovskites slows electron-hole recombination: time-domain *ab initio* analysis. *J. Phys. Chem. Lett.* 9, 1164–1171.
62. Kresse, G., and Furthmüller, J. (1996). Efficient iterative schemes for *ab initio* total-energy calculations using a plane-wave basis set. *Phys. Rev. B Condens. Matter* 54, 11169–11186.
63. Kresse, G., and Furthmüller, J. (1996). Efficiency of *ab initio* total energy calculations for metals and semiconductors using a plane-wave basis set. *Comput. Mater. Sci.* 6, 15–50.